

Wave propagation in media having negative permittivity and permeability

Richard W. Ziolkowski

Department of Electrical and Computer Engineering, University of Arizona, 1230 East Speedway Boulevard, Tucson, Arizona 85721-0104

Ehud Heyman

Department of Electrical Engineering—Physical Electronics, Tel-Aviv University, Tel-Aviv 69978, Israel

(Received 3 May 2001; published 30 October 2001)

Wave propagation in a double negative (DNG) medium, i.e., a medium having negative permittivity and negative permeability, is studied both analytically and numerically. The choices of the square root that leads to the index of refraction and the wave impedance in a DNG medium are determined by imposing analyticity in the complex frequency domain, and the corresponding wave properties associated with each choice are presented. These monochromatic concepts are then tested critically via a one-dimensional finite difference time domain (FDTD) simulation of the propagation of a causal, pulsed plane wave in a matched, lossy Drude model DNG medium. The causal responses of different spectral regimes of the medium with positive or negative refractive indices are studied by varying the carrier frequency of narrowband pulse excitations. The smooth transition of the phenomena associated with a DNG medium from its early-time nondispersive behavior to its late-time monochromatic response is explored with wideband pulse excitations. These FDTD results show conclusively that the square root choice leading to a negative index of refraction and positive wave impedance is the correct one, and that this choice is consistent with the overall causality of the response. An analytical, exact frequency domain solution to the scattering of a wave from a DNG slab is also given and is used to characterize several physical effects. This solution is independent of the choice of the square roots for the index of refraction and the wave impedance, and thus avoids any controversy that may arise in connection with the signs of these constituents. The DNG slab solution is used to critically examine the perfect lens concept suggested recently by Pendry. It is shown that the perfect lens effect exists only under the special case of a DNG medium with $\epsilon(\omega) = \mu(\omega) = -1$ that is both lossless and nondispersive. Otherwise, the closed form solutions for the field structure reveal that the DNG slab converts an incident spherical wave into a localized beam field whose parameters depend on the values of ϵ and μ . This beam field is characterized with a paraxial approximation of the exact DNG slab solution. These monochromatic concepts are again explored numerically via a causal two-dimensional FDTD simulation of the scattering of a pulsed cylindrical wave by a matched, lossy Drude model DNG slab. These FDTD results demonstrate conclusively that the monochromatic electromagnetic power flow through the DNG slab is channeled into beams rather than being focused and, hence, the Pendry perfect lens effect is not realizable with any realistic metamaterial.

DOI: 10.1103/PhysRevE.64.056625

PACS number(s): 41.20.Jb, 42.25.Bs, 42.79.Bh

I. INTRODUCTION

Several recent papers have exposed the usefulness of metamaterials that produce negative indices of refraction [1–7]. Metamaterials are artificially constructed materials having electromagnetic properties not generally found in nature. Examples include photonic band gap structures [2,8] and double negative (DNG) media [1,3–7], i.e., metamaterials having negative permittivity and negative permeability. Pendry [3] has proposed the intriguing possibility that a DNG medium could lead to a negative index of refraction and might overcome known problems with common lenses to achieve a “perfect” lens that would focus the entire spectrum, both the propagating as well as the evanescent spectra. Pendry’s analysis followed much of the original work of Veselago [1]. In this paper we use both analytical and numerical techniques to understand more completely the mathematics and wave physics associated with DNG medium propagation and scattering problems and apply the results to explore further this “perfect” lens concept.

In particular, we elucidate the choice of the square root

that leads to the negative angles associated with Snell’s law and the focusing effects Pendry associated with the DNG medium. Pendry’s analysis depends on a certain definition of the “forward” wave direction, as implied by a specific choice of the square root for the wave number and the wave impedance. Moreover, inconsistent choices for the propagating and evanescent spectra were made. We apply two well-known analytic continuation arguments to the choice of the square root. The ramifications of these choices are clarified in homogeneous DNG media and with the scattering of a plane wave from a DNG medium interface. Comparisons are achieved by defining correctly the sense of polarization; the field energies and satisfaction of Poynting’s theorem; and the reflection and transmission coefficients for both square root choices. This analysis also allows us, unlike Pendry, to define the square root consistently for the propagating and the evanescent spectra.

One-dimensional finite difference time domain (FDTD) simulations of the same DNG wave problems are given. The DNG medium is realized with lossy Drude models for both the electric permittivity and magnetic permeability. This

FDTD approach not only supports the steady state phenomena associated with the frequency domain analysis, but also demonstrates the causal transient behaviors. It is shown conclusively that the square root choice leading to a negative index of refraction and positive wave impedance is the correct one. The possibility of a negative index of refraction material that does not violate causality is also proved analytically and confirmed with these FDTD numerical experiments. The negative index result agrees with the recent work by Smith *et al.* [4–6]. However, there are some differences in the interpretation of the physics that we will elucidate. These include the concepts of causality, the power flow associated with the wave, and the polarization of the wave.

An analytical, exact frequency domain solution to the scattering of a wave from a DNG slab is given and is used to characterize several physical effects. In particular, it is used to critically examine the perfect lens concept suggested by Pendry. By studying in the frequency domain within a rigorous context a spectral analysis of the Green's function for the scattering of a plane wave from a DNG medium slab, we demonstrate conclusively that the solution is independent of the analytic continuation choices of the square root. Consequently, even though Pendry's analysis of the focusing of the evanescent spectrum [Eqs. (13)–(21) of [3]] is wrong because of the inconsistent choice of the square root, the final result that both the propagating and evanescent spectra are focused is correct. In fact, the derived closed form expression predicts two perfect foci: one at a point within the slab and one at a point beyond the slab. This agrees with the intuitive ray picture given in [3]; but, as we will demonstrate, care must be exercised in interpreting the meaning of the rays in the DNG slab. However, the exact solution also proves that this occurs for only one particular lossless, non-dispersive case for which the index of refraction is -1 , i.e., for a matched medium with $\epsilon(\omega)/\epsilon_0 = \mu(\omega)/\mu_0 = -1$ so that $n(\omega) = -1$. We find analytically that the perfect lens effect does not exist in general, particularly if the DNG medium has a large negative index or becomes lossy or dispersive. Rather, the waves in these more general DNG media are found to coalesce into, localized beam fields that channel the power flow.

Using two-dimensional FDTD simulations of the scattering of a line-source-generated cylindrical wave from a DNG slab realized with a double Drude medium, it is confirmed that the Pendry perfect lens effect does not occur in general. Moreover, we do find that, as predicted by the analytic solution, the DNG medium strongly channels the fields propagating in it in a paraxial sense along the propagation axis. The DNG slab acts like a converter from a pulsed cylindrical wave to a pulsed beam. This is demonstrated with simulations of the field intensity and the Poynting flux. As pointed out in [4], a realistic DNG material must in fact be dispersive. Consequently, the analytical and FDTD results demonstrate not only that Pendry's perfect lens effect is inaccessible with any metamaterial specially designed to realize the DNG medium, but also that such a metamaterial could be used to achieve the localized beam fields for a variety of applications.

II. PLANE WAVES IN A HOMOGENEOUS DOUBLE NEGATIVE MEDIUM

A. Time harmonic plane waves

Consider an x -polarized plane wave propagating along the z axis:

$$\mathbf{E} = [E_0, 0, 0]e^{ikz - i\omega t}, \quad (1a)$$

$$\mathbf{H} = [0, H_0, 0]e^{ikz - i\omega t}, \quad (1b)$$

the wave number k , the wave speed v , and the wave impedance Z being given by the expressions

$$k = \omega\sqrt{\epsilon\mu} = k_0 n, \quad n = \sqrt{\epsilon\bar{\mu}}, \quad (2)$$

$$v = \frac{\omega}{k} = \frac{1}{\sqrt{\epsilon\mu}} = \frac{c}{\sqrt{\epsilon\bar{\mu}}} = \frac{c}{n}, \quad (3)$$

$$Z = \frac{E_0}{H_0} = \frac{k}{\omega\epsilon} = \frac{1}{v\epsilon} = \sqrt{\frac{\mu}{\epsilon}} = \zeta Z_0, \quad \zeta = \sqrt{\bar{\mu}/\bar{\epsilon}}, \quad (4)$$

where the speed of light $c = 1/\sqrt{\epsilon_0\mu_0}$, the free space wave number $k_0 = \omega/c$, the free space wave impedance $Z_0 = \sqrt{\mu_0/\epsilon_0}$, the normalized permittivity $\bar{\epsilon} = \epsilon/\epsilon_0$, and the normalized permeability $\bar{\mu} = \mu/\mu_0$. The average Poynting's vector at the angular frequency ω corresponding to Eq. (1) is

$$\mathbf{S}_\omega = \frac{1}{2}\text{Re}(\mathbf{E} \times \mathbf{H}^*) = \hat{z} \frac{|E_0|^2}{2} \text{Re}\left(\frac{1}{Z^*}\right) e^{-2(\text{Im } k)z}. \quad (5)$$

The definitions of the wave speed and wave impedance consist of square roots whose proper signs need to be defined. This subject will be dealt with in Secs. (II B)–(II D). We note, though, from the expressions for Z that the sign of the square root in Z is uniquely defined by k . Furthermore, defining the wave vector $\mathbf{k} = \hat{k}k$ by introducing the direction of propagation \hat{k} (where here $\hat{k} = \hat{z}$), then regardless of the definitions of these square roots we have for the DNG medium

$$\mathbf{E}_0 \perp \mathbf{H}_0 \perp \text{Re } \mathbf{k} \quad \text{and} \quad \mathbf{S}_\omega \cdot \text{Re } \mathbf{k} < 0. \quad (6)$$

To avoid confusion with the terminology associated with chiral (left- or right-handed) materials, we will call a plane wave that has $\mathbf{S}_\omega \cdot \text{Re } \mathbf{k} \leq 0$ simply a LH or a RH plane wave, respectively. The LH plane wave terminology was introduced in [1] for the case, for example, in which the wave propagates in the \hat{k} direction but has \mathbf{E} , \mathbf{H} , and $\text{Re } \mathbf{k}$ forming a left-handed coordinate system so that $\mathbf{S}_\omega \cdot \text{Re } \mathbf{k} < 0$ as opposed to a right-handed system for which this projection would be positive.

The definition of the square roots in Eqs. (2)–(4) affects the field structure described by Eq. (1) and the power flow

described by Eq. (5). Again, note that the sign of the square root for ζ depends on the sign chosen for n , i.e., they are not independent.

Henceforth we shall consider two alternative definitions of the square roots that are based upon analytic continuation considerations. It is found that physically based expressions for the electromagnetic waves can be obtained that are independent of either of the analytic continuation definitions. The question of what is the proper definition of a square root is then replaced with the question of what is the ‘‘outgoing’’ wave direction. This question becomes critical in problems involving transitions through interfaces since, in order to define the reflection and transmission coefficients, one needs to define the ‘‘incoming’’ and the ‘‘outgoing’’ solutions with respect to the interface.

B. Definitions of the square roots

In a DNG medium, the relative constitutive parameters satisfy

$$\bar{\epsilon} = |\bar{\epsilon}|e^{i\phi_\epsilon}, \quad \phi_\epsilon \in (\pi/2, \pi], \quad (7a)$$

$$\bar{\mu} = |\bar{\mu}|e^{i\phi_\mu}, \quad \phi_\mu \in (\pi/2, \pi]. \quad (7b)$$

Expressing

$$n = |n|e^{i\phi_n}, \quad \zeta = |\zeta|e^{i\phi_\zeta}, \quad (8)$$

one choice for the square roots in Eqs. (2)–(4) is

$$\phi_n = \frac{1}{2}(\phi_\mu + \phi_\epsilon) \in (\pi/2, \pi], \quad (9a)$$

$$\phi_\zeta = \frac{1}{2}(\phi_\mu - \phi_\epsilon) \in (-\pi/4, \pi/4), \quad (9b)$$

while the alternative choice is

$$\phi_n = \frac{1}{2}(\phi_\mu + \phi_\epsilon) - \pi \in (-\pi/2, 0], \quad (10a)$$

$$\phi_\zeta = \frac{1}{2}(\phi_\mu - \phi_\epsilon) + \pi \in (3\pi/4, 5\pi/4). \quad (10b)$$

For small loss we may obtain explicit expressions for n and ζ . Expressing $\bar{\epsilon} = \bar{\epsilon}_r + i\bar{\epsilon}_i$ and $\bar{\mu} = \bar{\mu}_r + i\bar{\mu}_i$, we find that, if

$$0 \leq \bar{\epsilon}_i \ll |\bar{\epsilon}_r| \quad \text{and} \quad 0 \leq \bar{\mu}_i \ll |\bar{\mu}_r|, \quad (11)$$

then

$$n \approx \mp \sqrt{|\bar{\epsilon}_r \bar{\mu}_r|} \left[1 - i \frac{1}{2} \left(\frac{\bar{\epsilon}_i}{|\bar{\epsilon}_r|} + \frac{\bar{\mu}_i}{|\bar{\mu}_r|} \right) \right], \quad (12a)$$

$$\zeta \approx \pm \sqrt{|\bar{\mu}_r / \bar{\epsilon}_r|} \left[1 - i \frac{1}{2} \left(\frac{\bar{\mu}_i}{|\bar{\mu}_r|} - \frac{\bar{\epsilon}_i}{|\bar{\epsilon}_r|} \right) \right], \quad (12b)$$

and in the lossless limit

$$n = \mp \sqrt{|\bar{\epsilon}_r \bar{\mu}_r|}, \quad \zeta = \pm \sqrt{|\bar{\mu}_r / \bar{\epsilon}_r|}. \quad (13)$$

The upper and lower signs in Eqs. (12) and (13) correspond to the definitions in Eqs. (9) and (10), respectively. Explicitly, note that with Eq. (9) $\text{Re } \zeta > 0$, $\text{Re } n < 0$, and $\text{Im } n > 0$ and with Eq. (10) $\text{Re } \zeta < 0$, $\text{Re } n > 0$, and $\text{Im } n < 0$. Thus, note that with Eq. (10), the wave is LH with respect to both the wave vector \mathbf{k} and the direction of propagation $\hat{\mathbf{z}}$, but with Eq. (9), the wave is LH with respect to the wave vector and RH with respect to $\hat{\mathbf{z}}$. This issue will arise when we discuss the power and energy results associated with Poynting’s theorem.

C. The wave directions

The effects of the definitions of the square roots are best characterized by their effects on the direction of causality, the wave directions associated with reflection and transmission from an interface, and the electromagnetic power flow associated with both concepts. Such a discussion introduces a general characterization of plane wave properties and relies on Poynting’s theorem, which gives a relation between the time variation of the field energy in a region of space and the power flux through the surface surrounding that region.

We summarize the plane wave properties by considering the direction of the Poynting vector \mathbf{S}_ω in Eq. (5) versus the direction $\hat{\mathbf{v}}$ of $\text{Re } \mathbf{k}$, i.e., the direction of increase of the real part of the phase.

Applying the root in Eq. (10) to the solution in Eqs. (1)–(4) we see that $\hat{\mathbf{v}} = +\hat{\mathbf{z}}$ while \mathbf{S}_ω of Eq. (5) points in the $-\hat{\mathbf{z}}$ direction, which is also the direction of exponential decay of the wave due to the loss term in \mathbf{k} . Applying instead the root in Eq. (9), we see that $\hat{\mathbf{v}} = -\hat{\mathbf{z}}$ while \mathbf{S}_ω of Eq. (5) points in the $+\hat{\mathbf{z}}$ direction, which is also the direction of exponential decay of the wave. In both cases the solution is LH with respect to $(\mathbf{E}_0, \mathbf{H}_0, \hat{\mathbf{v}})$ and hence $\mathbf{S}_\omega \cdot \hat{\mathbf{v}} < 0$.

D. Causal medium

Since the choice of the square root defines the causal properties of the wave solution, one has to explore the analytic properties of the dispersion relation $k(\omega)$ over the entire frequency domain as implied by the requirement that the medium will be causal. Causality in a linear dispersive medium implies that if $\epsilon(\omega)$ and $\mu(\omega)$ are transformed to the time domain via the inverse Fourier transformation

$$F(t) = \frac{1}{2\pi} \int_{-\infty}^{\infty} d\omega f(\omega) e^{-i\omega t} \quad (14)$$

then their time domain counterparts $\epsilon(t)$ and $\mu(t)$ are strictly causal in the sense that $\epsilon(t) = 0$ and $\mu(t) = 0$ for $t < 0$ (for simplicity we do not introduce special symbols for time domain constituents, and we use the time variable t explicitly whenever confusion may occur). Since in addition the time domain solutions are real, it follows that the frequency domain constitutive parameters should satisfy

$$\epsilon(-\omega) = \epsilon^*(\omega), \quad \mu(-\omega) = \mu^*(\omega) \quad \text{for real } \omega, \quad (15a)$$

$$\epsilon(\omega) \text{ and } \mu(\omega) \text{ are analytic functions for } \text{Im } \omega \geq 0, \quad (15b)$$

$$|\omega[\epsilon(\omega) - \epsilon_0]| \rightarrow 0 \quad \text{and} \quad |\omega[\mu(\omega) - \mu_0]| \rightarrow 0$$

as $|\omega| \rightarrow \infty$ for $\text{Im } \omega \geq 0$. (15c)

Thus all the singularities (poles and branch points and the associated branch cuts) of $\epsilon(\omega)$ and $\mu(\omega)$ must lie in $\text{Im } \omega < 0$. Furthermore, the function $n(\omega)$ and, thereby, $Z(\omega)$ in Eqs. (3) and (4) should be analytic in $\text{Im } \omega \geq 0$ (i.e., the branch cut introduced by the square root there should be in $\text{Im } \omega < 0$).

As an example, consider the lossy Drude medium, suggested in [3] in connection with the DNG slab

$$\epsilon(\omega) = \epsilon_0 \left(1 - \frac{\omega_{pe}^2}{\omega(\omega + i\Gamma_e)} \right), \quad (16a)$$

$$\mu(\omega) = \mu_0 \left(1 - \frac{\omega_{pm}^2}{\omega(\omega + i\Gamma_m)} \right). \quad (16b)$$

We provide a slight variation of this for discussion purposes:

$$\epsilon(\omega) = \epsilon_0 \left(1 - \frac{\omega_{pe}^2}{(\omega + i\Gamma_{e1})(\omega + i\Gamma_{e2})} \right), \quad (17a)$$

$$\mu(\omega) = \mu_0 \left(1 - \frac{\omega_{pm}^2}{(\omega + i\Gamma_{m1})(\omega + i\Gamma_{m2})} \right), \quad (17b)$$

where all the Γ coefficients are positive to ensure analyticity in $\text{Im } \omega \geq 0$ and represent losses that may be taken to be small. These models are actually Lorentz medium models, e.g.,

$$\epsilon_L(\omega) = \epsilon_0 \left(1 + \frac{\omega_{pe}^2}{-\omega^2 - i\Gamma_e \omega + \omega_{0e}^2} \right), \quad (18)$$

where $\Gamma_e = \Gamma_{e1} + \Gamma_{e2}$ and $\omega_{0e}^2 = \Gamma_{e1}\Gamma_{e2}$. One readily verifies that $\text{Re } \epsilon_L < 0$ for ω roughly smaller than ω_{pe} , with $\text{Im } \epsilon_L > 0$ ($\text{Im } \epsilon_L > 0$ is relatively small for real ω if the Γ coefficients are small). A similar relation applies for μ and its imaginary part.

As discussed above, $\sqrt{\epsilon}$ and $\sqrt{\mu}$ should be analytic in $\text{Im } \omega \geq 0$. Thus, choosing the positive root for $\omega \gg \omega_{pe}, \omega_{pm}$ [i.e., $\sqrt{\epsilon} \rightarrow \sqrt{\epsilon_0}$ and $\sqrt{\mu} \rightarrow \sqrt{\mu_0}$ as implied by Eq. (15c)] and then continuing the square root analytically along the real axis (more generally, in $\text{Im } \omega \geq 0$) to the regions $\omega < \omega_{pe}, \omega_{pm}$, where ϵ and μ are approximately negative (with small positive imaginary part), one finds there that

$\sqrt{\epsilon(\omega)} \approx +i\sqrt{|\epsilon(\omega)|}$ and $\sqrt{\mu(\omega)} \approx +i\sqrt{|\mu(\omega)|}$. This implies that square roots for v and Z in this range are described properly by Eq. (9).

E. Energy and power

As noted in [7] and by many others, the correct form of Poynting's theorem in a dispersive medium is [9]

$$-\int_{\Sigma=\partial V} \mathbf{S} \cdot \hat{\mathbf{n}}_{\Sigma} d\Sigma = \int_V [\epsilon_0 \mathbf{E} \cdot \partial_t \mathbf{E} + \mathbf{E} \cdot \partial_t \mathbf{P} + \mu_0 \mathbf{H} \cdot \partial_t \mathbf{H} + \mu_0 \mathbf{H} \cdot \partial_t \mathbf{M}] dV, \quad (19)$$

where the volume V is bounded by the surface $\Sigma = \partial V$, which has the unit outward-pointing normal $\hat{\mathbf{n}}_{\Sigma}$. The form of Poynting's theorem in a homogenous, nondispersive medium is

$$-\int_{\Sigma=\partial V} \mathbf{S} \cdot \hat{\mathbf{n}}_{\Sigma} d\Sigma = \partial_t \int_V \left[\frac{1}{2} \epsilon |\mathbf{E}|^2 + \frac{1}{2} \mu |\mathbf{H}|^2 \right] dV = \partial_t U_{em}. \quad (20)$$

Discrepancies between Eqs. (19) and (20) are immediately apparent. In a homogeneous, nondispersive DNG medium, the quantity U_{em} in Eq. (20) is negative. Thus, if an electromagnetic field enters a DNG region, the right-hand side (RHS) of Eq. (20) is then negative. In contrast, the RHS of Eq. (19) is expected to be positive if the polarization and magnetization fields are in the same direction as the electric and magnetic fields, as they would be in the case of the Drude medium. As pointed out in [4], the DNG medium has to be dispersive so one should use Eq. (19) in any considerations of the power flow for that case.

In addition, because the two square root choices lead to different results for the left-hand side (LHS) of either Eq. (19) or Eq. (20), the power flow into the medium becomes another identifier of the correct choice of the square root. In particular, let the volume V be a large semi-infinite space in the x - y directions. Let the entrance face to this region be the plane $z=0$ and let the exit face be $z=\infty$ so that for a finite time the pulse has no interactions with the exit face. Since $\hat{\mathbf{n}}_{\Sigma} = -\hat{\mathbf{z}}$ is the outward-pointing normal on the entrance face, Eq. (9) gives a LH plane wave with respect to \mathbf{k} that is propagating in the $\hat{\mathbf{k}} = +\hat{\mathbf{z}}$ direction and gives a positive power flow (negative flux) into the volume V . On the other hand, Eq. (10) gives a LH plane wave that will have negative power flow into the volume V through the surface Σ because its flux is positive.

F. Interface and slab problems

From the discussions in previous sections it follows that the behavior of the wave scattered from a DNG interface or slab can serve as another indicator of the correct choice of the square root. We therefore pay special attention to these examples, both analytically and numerically.

The reflection and transmission coefficients for a wave impinging normally from the free space side on a DNG interface are given by

$$r_{01} = \frac{Z - Z_0}{Z + Z_0}, \quad t_{01} = 1 + r_{01} = \frac{2Z}{Z + Z_0}. \quad (21)$$

Consider, for example, a ‘‘matched medium’’ where $\bar{\epsilon} = \bar{\mu}$. For the choice of k in Eq. (9), we obtain $Z = Z_0$ and $r_{01} = 0$. We also obtain for this case that S_ω of the transmitting wave in the DNG medium propagates away from the interface, but the phase of this wave decreases away from the interface so that the wave on the DNG side seems to be propagating *toward* the interface. For the choice in Eq. (10), on the other hand, the phase of the transmitted wave increases (propagates) away from the interface but S_ω propagates toward the interface. Furthermore, in this case we have $Z = -Z_0$; hence, r_{01} and t_{01} blow up.

The fact that r_{01} and t_{01} blow up does not rule out the choice of the square root in Eq. (10) since this special case can be treated in a proper limit sense. For the DNG slab, the series of multiple internal interactions can be summed up in closed form even in this pathological limit and the final result provides a regular expression for the field which is given in Eqs. (43) and (46) below. It should be pointed out that this final result is, in fact, independent of the choice of the square root in either Eq. (9) or Eq. (10). Thus in order to address the issue of the ‘‘correct’’ or ‘‘physical’’ choice for the square root it is suggested to study first the problem of an interface with a matched DNG under transient excitation. Consequently, one-dimensional (1D) time domain simulations of both the one-dimensional interface and slab cases are considered in this regard next.

III. 1D FDTD SIMULATIONS OF THE DNG INTERFACE AND SLAB PROBLEMS

With the square root choices and their consequences in hand, we simulated the interaction of a plane wave with the DNG slab in 1D and the interaction of a line source field with a DNG slab in 2D using a finite difference time domain simulator [10,11]. The DNG slab was modeled by the lossy Drude medium (16). These material models are incorporated into a standard FDTD simulator with the corresponding auxiliary differential equations for the polarization and magnetization currents. As noted previously, the Drude DNG medium modeled with the FDTD simulator is temporally dispersive. However, there is no loss in generality in the results for the choice of the square root. Moreover, this auxiliary material approach allows one to isolate the medium physics from the field physics for postprocessing purposes. Note that there is no possibility of inserting a constant negative permittivity or permeability into a leapfrog staggered grid FDTD simulator and having it run stably.

We considered a low loss, matched DNG medium with $\omega_{pe} = \omega_{pm} = \omega_p$ and $\Gamma_e = \Gamma_m = \Gamma$ so that $\bar{\epsilon} = \bar{\mu} = 1 + \chi$. Plots of $\text{Re}(1 + \chi)$ and $\text{Im}(1 + \chi)$ for $\Gamma = 1.0 \times 10^8$ rad/s when

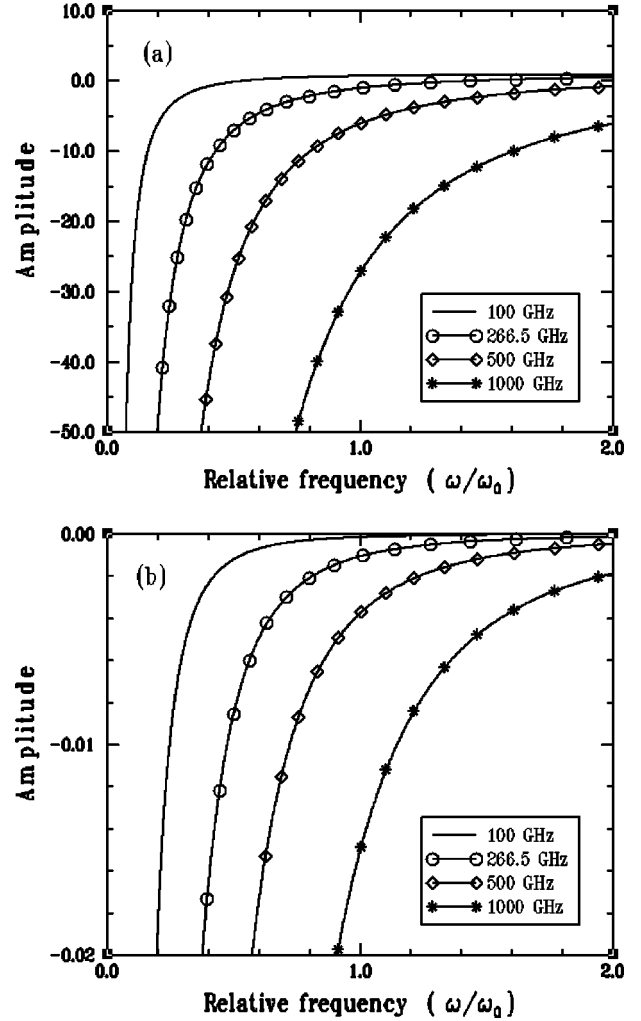


FIG. 1. (a) Real part of the relative Drude ϵ, μ model for the angular plasma frequency $\omega_p = 1.0 \times 10^{11}$ rad/s, $\omega_p = 2.665 \times 10^{11}$ rad/s, $\omega_p = 5.0 \times 10^{11}$ rad/s, $\omega_p = 1.0 \times 10^{12}$ rad/s where $\Gamma = 1.0 \times 10^8$ rad/s. (b) Imaginary part of the relative Drude ϵ, μ model for the angular plasma frequency $\omega_p = 1.0 \times 10^{11}$ rad/s, $\omega_p = 2.665 \times 10^{11}$ rad/s, $\omega_p = 5.0 \times 10^{11}$ rad/s, $\omega_p = 1.0 \times 10^{12}$ rad/s where $\Gamma = 1.0 \times 10^8$ rad/s.

$\omega_p = 1.0 \times 10^{11}$ rad/s, $\omega_p = 2.665 \times 10^{11}$ rad/s, $\omega_p = 5.0 \times 10^{11}$ rad/s, and $\omega_p = 1.0 \times 10^{12}$ rad/s are given, respectively, in Figs. 1(a) and 1(b). The angular frequency has been normalized to the target frequency $\omega_0 = 2\pi f_0$, where $f_0 = 30$ GHz. This target frequency value f_0 was chosen arbitrarily. All of the results can be achieved in a similar fashion at any set of microwave, millimeter, or optical frequencies with the appropriate frequency values in the Drude models. As shown in Fig. 1(a), the case with $\omega_p = 1.0 \times 10^{11}$ rad/s does not produce a DNG medium at the target frequency, while the cases with $\omega_p = 2.665 \times 10^{11}$ rad/s, $\omega_p = 5.0 \times 10^{11}$ rad/s, and $\omega_p = 1.0 \times 10^{12}$ rad/s do. In particular, the values of $\text{Re}(1 + \chi)$ at the target frequency are approximately -1.0 , -6.0 , and -27.0 . As shown in Fig. 1(b), the losses in all cases are small in comparison to the real parts.

A. 1D FDTD simulations

The 1D time domain equations solved with the FDTD simulator for the matched DNG medium were

$$\begin{aligned}\partial_t E_x &= \frac{1}{\epsilon_0} (-\partial_z H_y - J_x), \\ \partial_t J_x + \Gamma J_x &= \epsilon_0 \omega_p^2 E_x, \\ \partial_t H_y &= \frac{1}{\mu_0} (-\partial_z E_x - K_y), \\ \partial_t K_y + \Gamma K_y &= \mu_0 \omega_p^2 H_y,\end{aligned}\quad (22)$$

where K_y has been normalized by μ_0 to make the magnetic current equation dual to the electric current definition. These equations are discretized with the standard staggered grid, leapfrog in time approach. The electric field is taken at the cell edge for integer time steps; the magnetic field is taken at the cell center for half-integer time steps. The electric and magnetic currents were located together at the cell centers in order to achieve the matched medium conditions numerically. This required averaging of the electric field and electric current values in the discrete equations. If $E_x^n(i) = E_x(i\Delta z, n\Delta t)$, $J_x^{n+1/2}(i+1/2) = J_x((i+1/2)\Delta z, (n+1/2)\Delta t)$, $H_y^{n+1/2}(i+1/2) = H_y((i+1/2)\Delta z, (n+1/2)\Delta t)$, and $K_y^n(i+1/2) = K_y((i+1/2)\Delta z, n\Delta t)$, the discretized equations in the FDTD simulator are

$$\begin{aligned}H_y^{n+1/2}(i+1/2) &= H_y^{n-1/2}(i+1/2) - \frac{\Delta t}{\mu_0 \Delta z} [E_x^n(i+1) - E_x^n(i) \\ &\quad + K_y^n(i+1/2)\Delta z], \\ K_y^{n+1}(i+1/2) &= \frac{1-0.5\Gamma\Delta t}{1+0.5\Gamma\Delta t} K_y^n(i+1/2) \\ &\quad + \frac{\mu_0 \omega_p^2 \Delta t}{1+0.5\Gamma\Delta t} H_y^{n+1/2}(i+1/2), \\ E_x^{n+1}(i) &= E_x^n(i) - \frac{\Delta t}{\epsilon_0 \Delta z} \left\{ [H_y^{n+1/2}(i+1/2) - H_y^{n+1/2}(i-1/2)] \right. \\ &\quad \left. + \frac{1}{2} [J_x^{n+1/2}(i+1/2) + J_x^{n+1/2}(i-1/2)] \Delta z \right\}, \\ J_x^{n+3/2}(i+1/2) &= \frac{1-0.5\Gamma\Delta t}{1+0.5\Gamma\Delta t} J_x^{n+1/2}(i+1/2) \\ &\quad + \frac{1}{2} \frac{\epsilon_0 \omega_p^2 \Delta t}{1+0.5\Gamma\Delta t} [E_x^{n+1}(i) + E_x^{n+1}(i+1)].\end{aligned}\quad (23)$$

The initial field is launched from a total-field/scattered-field (TF-SF) plane within the mesh [10]. Two types of unit amplitude pulse were used. One was a single cycle, broad bandwidth pulse

$$f(t) = \begin{cases} \sqrt{7.0}(7.0/6.0)^3 \times \left(\frac{t-T_p/2}{T_p/2} \right) \times \left[1 - \left(\frac{t-T_p/2}{T_p/2} \right)^2 \right]^3 & \text{for } 0 \leq t \leq T_p \\ 0 & \text{for } t > T_p, \end{cases}\quad (24)$$

where T_p is the length of time the pulse has a nonzero value. This single cycle pulse has a broad bandwidth, and the peak of its frequency spectrum occurs at $f_0 = 1/T_p$. The other input signal is the multiple cycle m - n - m pulse:

$$f(t) = \begin{cases} g_{on}(t) \sin(\omega_0 t) & \text{for } 0 \leq t < mT_p \\ \sin(\omega_0 t) & \text{for } mT_p \leq t \leq (m+n)T_p \\ g_{off}(t) \sin(\omega_0 t) & \text{for } (m+n)T_p < t \leq (m+n+m)T_p \\ 0 & \text{for } t > (m+n+m)T_p, \end{cases}\quad (25)$$

where $T_p = 2\pi/\omega_0 = 1/f_0$ is the period of one cycle and the three-derivative smooth window functions are given by the expressions

$$\begin{aligned}g_{on}(t) &= 10.0x_{on}^3 - 15.0x_{on}^4 + 6.0x_{on}^5, \\ g_{off}(t) &= 1.0 - [10.0x_{off}^3 - 15.0x_{off}^4 + 6.0x_{off}^5],\end{aligned}\quad (26)$$

where $x_{on} = 1.0 - (mT_p - t)/mT_p$ and $x_{off} = [t - (m+n)T_p]/mT_p$. The m - n - m pulse is a sinusoidal signal that has a smooth windowed turn-on for m cycles, a constant amplitude for n cycles, and then a smooth windowed turn-off for m cycles; hence, it has an adjustable bandwidth (through the total number of cycles $m+n+m$) centered at the frequency f_0 . For the cases considered below, either a 20-cycle, 5-10-5 pulse or a cw signal (5-1000-5 pulse) was used to probe the DNG slab.

The 1D FDTD grid was terminated at both ends with a one-way wave operator absorbing boundary condition. For a Courant number $c\Delta t/\Delta z = 1.0$, this is an exact truncation. The Courant number must be less than or equal to 1 for the FDTD simulator to be stable for free space problems. When the Drude model is included, the Courant condition is more complicated but is well known. A recent review [12] discusses the various discretization schemes for a variety of dispersive media.

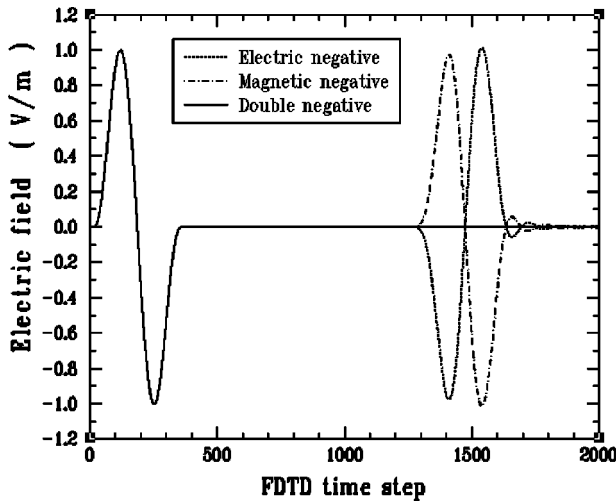


FIG. 2. The time histories of the electric field E_x measured in front of the total field/scattered field plane for a negative permittivity medium, a negative permeability medium, and a DNG medium.

Unless otherwise noted, the 1D FDTD problem space for the simulation results discussed below was taken to be 5000 cells long where $\Delta z = 3.0 \times 10^{-5} \text{ m} = \lambda_0/300$ where the target frequency $f_0 = c/\lambda_0 = 30.0 \text{ GHz}$. The corresponding time step was $\Delta t = 0.95 \Delta z/c = 9.5 \times 10^{-14} \text{ s} = 95 \text{ fs}$. The total field/scattered field plane was set at $z = i\Delta z$ where $i = 600$; the front face of the DNG slab at $z = i\Delta z$ where $i = 1200$; and the back face of the DNG slab at $z = i\Delta z$ where either $i = 1800$ or $i = 2400$. Thus, the DNG slab was 600 or 1200 cells thick. The slab was defined by the DNG cases shown in Figs. 1.

B. DNG medium results

First, the matched nature of the FDTD equations (23) was tested with a simple interface problem. The single cycle pulse was launched toward a 600-cell slab that had negative permittivity only, negative permeability only, and both negative permittivity and permeability. The E_x field was measured at $i = 610$, 10 cells in front of the TF-SF plane. The results are shown in Fig. 2. The incident pulse appears on the left, the reflected pulses on the right. The measured electric field has the correct, opposite polarities for the single negative parameter cases. The reflected pulse in the DNG case was 1.5×10^{-4} smaller than the incident field, essentially at the expected ‘‘matched’’ level for the discretization used.

Next, the propagation characteristics of the pulses in the DNG were investigated. Several quantities were measured in the 600-cell DNG slab case. The term $E_x H_y$ was measured in time at three points $i = 1205, 1500, 1795$. The energy quantity $\int E_x H_y \Delta t$ was measured just in front of the TF-SF plane at $i = 610$ and just after the slab at $i = 1810$. The results for $E_x H_y$ for the 20-cycle incident pulse are shown in Fig. 3; those for the energy quantity $\int E_x H_y \Delta t$ are shown in Fig. 4. The energy calculation for a 1200-cell DNG slab is also provided in Fig. 4 as is the free space result. From Fig. 3 we found that $E_x H_y$ was positive. The wave in the DNG slab was definitely LH with respect to \mathbf{k} , but RH with respect to

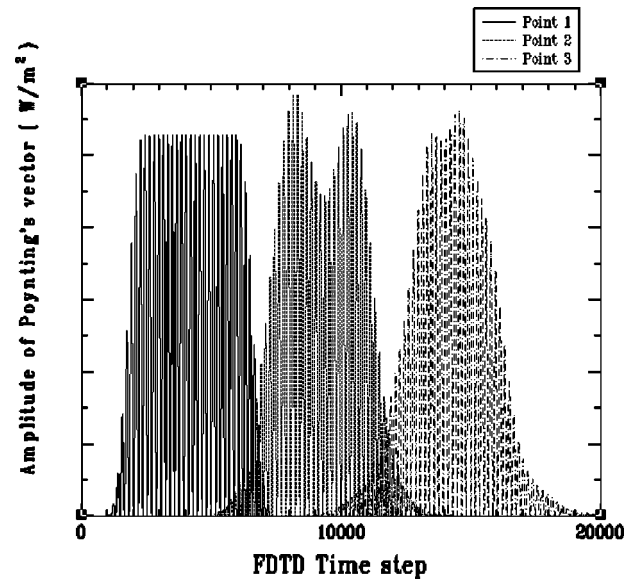


FIG. 3. The time history of the Poynting vector term $E_x H_y$ was measured at three points in the DNG medium.

the direction of propagation \hat{z} . Although there is some peaking in Fig. 3, the term $E_x H_y$ decreases in the DNG slab. This was tested further with the cw incident pulse. The steady state values for the term $E_x H_y$ were successively less at each of the three observation points. This is confirmed in Fig. 4. The DNG medium is lossy and does absorb some of the energy. There is no gain in the signals. The peaks in Fig. 3 are due to the ‘‘turn-on’’ and ‘‘turn-off’’ portions of the incident pulse. These broad bandwidth components have different propagation characteristics from the main part of the pulse as confirmed by the cw runs.

Figure 4 also demonstrates that the DNG medium slows down the propagation speed of the pulse considerably. The

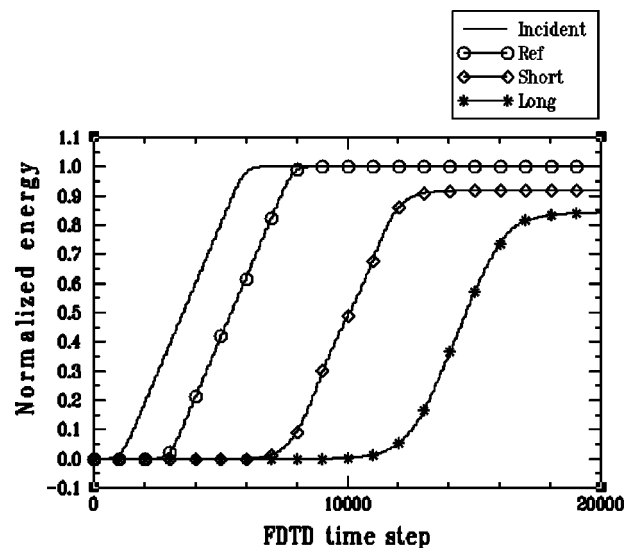


FIG. 4. The energy received at a fixed observation point behind the DNG slab is plotted as a function of the simulation time. Values for thin and thick slabs are compared to reference values. The DNG medium can dramatically slow down a wave propagating through it.

steady state wave front propagates at the group velocity of the target frequency f_0 . In particular, the general formula for the group velocity is

$$v_g(\omega) = [\partial_\omega k]^{-1} = c[\partial_\omega(\omega n(\omega))]^{-1} \quad (27a)$$

$$= \left[\frac{c}{n} \right] \left[1 + \frac{\omega}{2} \left(\frac{\partial_\omega \chi_e}{\bar{\epsilon}} + \frac{\partial_\omega \chi_m}{\bar{\mu}} \right) \right]^{-1}, \quad (27b)$$

where in the last expression the susceptibility terms $\bar{\epsilon} = 1 + \chi_e$ and $\bar{\mu} = 1 + \chi_m$ have been used. Note also that the phase velocity $v_p = c/n(\omega)$. For the Drude DNG (17), we have

$$v_g(\omega) = \left[\frac{c}{n} \right] \left[1 + \frac{\omega_{pe}^2(\omega + i\Gamma_e/2)}{\omega(\omega + i\Gamma_e)^2 \bar{\epsilon}} + \frac{\omega_{pm}^2(\omega + i\Gamma_m/2)}{\omega(\omega + i\Gamma_m)^2 \bar{\mu}} \right]^{-1} \quad (28a)$$

$$\approx \left[\frac{c}{n} \right] \left[1 + \frac{\omega_{pe}^2}{\omega^2 \bar{\epsilon}} + \frac{\omega_{pm}^2}{\omega^2 \bar{\mu}} \right]^{-1}, \quad (28b)$$

where the last approximation applies if the loss term is small, i.e., $\omega \gg \Gamma_{e,m}$. For our target frequency f_0 , since $\bar{\epsilon}, \bar{\mu} \ll -1$ for $\omega < \omega_p$, we have $\omega_{pe}^2/\omega^2 \gg 2$; hence, one verifies that $v_g(\omega) > 0$ (i.e., it is in the $+z$ direction) and that $|v_g(\omega)| \ll |c/n|$ (i.e., it is very slow). In fact, for the low loss, matched DNG medium with $\bar{\epsilon} = \bar{\mu}$, one has approximately that

$$v_g(\omega) \approx c \left[1 + \frac{\omega_p^2}{\omega^2} \right]^{-1}. \quad (29)$$

For the 2.665×10^{11} rad/s, 5.0×10^{11} rad/s, and 1.0×10^{12} rad/s DNG media, the wave group speed (29) is, respectively, $0.3334c$, $0.124c$, and $0.0343c$. A precise measure of the speed from the simulation results is quite difficult. Here, it is desired to avoid the earliest time points since the envelope of the excitation pulse contains a variety of high frequency components whereas late times require dealing with issues of the medium's relaxation rate. Selecting the point on the curves in Fig. 4 at which 50% of the energy has been collected at the observation point, one finds that the difference in the number of time steps between the reference and the short DNG slab is $4412\Delta t$, and for the long DNG slab is $8901\Delta t$. The expected values were $(600/0.124 - 600)\Delta t/0.95 = 4462\Delta t$ and $(1200/0.124 - 1200)\Delta t/0.95 = 8924\Delta t$. The difference between the analytical and the numerical times is $\sim 0.26\%$; hence, the agreement is very good.

No change in the direction of causality was observed in the 1D FDTD simulation results; only propagation in the forward direction was observed in the slabs for time prior to the waves interacting with the back side of the DNG slab. Moreover, since the slab was matched to free space, no reflections from this back side of the DNG slab were observed. The wave simply slowed down in the DNG slab and finally made its way out of it.

To further confirm the signs of Poynting's vector and the energy, several more quantities were calculated. In particular, by calculating $\mathbf{P} = \int \mathbf{J} \Delta t$ and $\mu_0 \mathbf{M} = \int \mathbf{K} \Delta t$, the RHS of Eq. (20) was calculated for the DNG slab as

$$U_{em} = (1/2) \int_0^{600\Delta z} [(\epsilon_0 \mathbf{E} + \mathbf{P}) \cdot \mathbf{E} + \mu_0 (\mathbf{H} + \mathbf{M}) \cdot \mathbf{H}] dz. \quad (30)$$

As expected, the energy U_{em} was found to be negative over the extent of the pulse duration. The corresponding result for the RHS of Eq. (19) for the $600\Delta z$ DNG slab under consideration becomes

$$- [E_x H_y]_{z=1200\Delta z}^{z=1800\Delta z} = \int_0^{600\Delta z} [\epsilon_0 \mathbf{E} \cdot \partial_t \mathbf{E} + \mathbf{E} \cdot \partial_t \mathbf{P} + \mu_0 \mathbf{H} \cdot \partial_t \mathbf{H} + \mu_0 \mathbf{H} \cdot \partial_t \mathbf{M}] dz. \quad (31)$$

The calculated results are shown in Fig. 5 for the 20-cycle pulse excitation of the $\omega_p = 5.0 \times 10^{11}$ rad/s, $\Gamma = 1.0 \times 10^8$ rad/s slab. The power in the medium as calculated by the LHS of Eq. (31) will be labeled P_{LHS} ; it is the negative of the difference in the flux through the DNG slab. The results for this quantity are given in Fig. 5(a). Notice that P_{LHS} is positive across the entrance face, but negative across the exit face. This can occur only if $E_x H_y$ is a positive quantity. The ability to distinguish the powers across the two faces occurs because the wave speed in the DNG slab is so slow. On the other hand, let the power in the medium as calculated by the RHS of Eq. (31) be labeled P_{RHS} . Let the maximum instantaneous value of P_{LHS} be P_{max}^{LHS} . The normalized square difference between these two power calculations,

$$\left[\frac{P_{RHS} - P_{LHS}}{P_{max}^{LHS}} \right]^2, \quad (32)$$

is shown in Fig. 5(b). Despite the spatial integration (averaging) and the time derivatives associated with P_{RHS} , its predicted values agree quite precisely with the instantaneous power flow difference calculations. Moreover, both expressions yield positive power values in the DNG slab. This further confirms the fact that the wave in the DNG medium is LH with respect to $\hat{\mathbf{k}}$ but RH with respect to the direction of propagation $\hat{\mathbf{z}}$. Positive energy flows into the DNG medium to cause the term $-\partial_t U_{em}$ to increase; i.e., if we let the DNG medium's permittivity and permeability exhibit small losses, then we have the result that the power flow is increasing as the wave enters the medium while the energy density becomes more negative. This has been previously confirmed numerically for related media in [7].

C. Index of refraction

Finally, the relationship between the causal propagation and the negative index of refraction predictions for the DNG medium was considered. The negative index was also calcu-

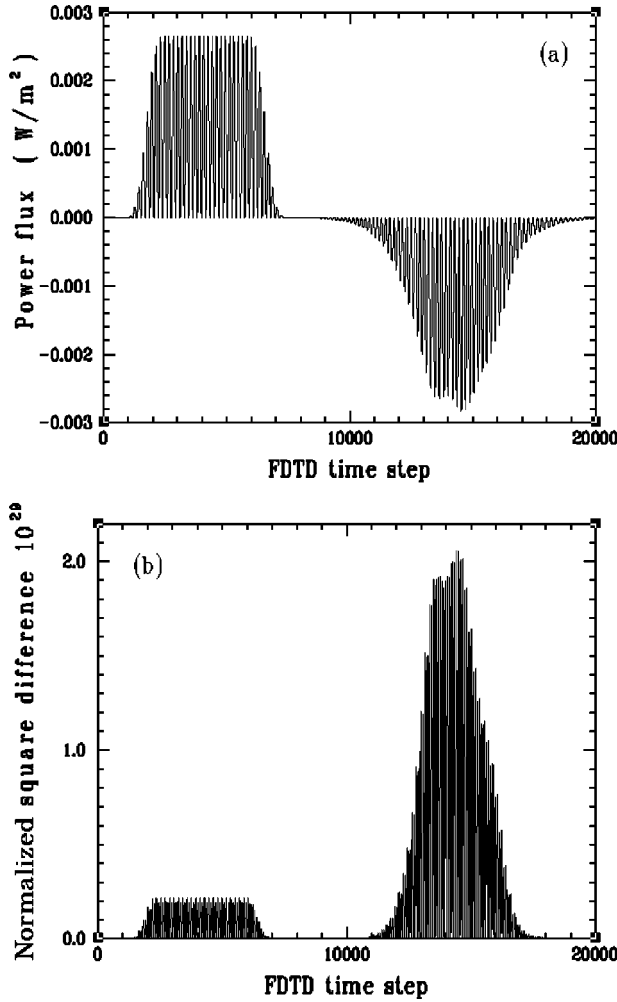


FIG. 5. (a) The negative flux of the instantaneous Poynting vector through the DNG slab with $\omega_p = 5.0 \times 10^{11}$ rad/s and $\Gamma = 1.0 \times 10^8$ rad/s is plotted against the number of FDTD time steps for the 20-cycle pulse excitation. (b) Normalized square difference between the negative flux of the instantaneous Poynting vector through the slab and the integrated local power density in the same slab.

lated explicitly. The cw was driven into a DNG medium with $\omega_p = 2.665 \times 10^{11}$ rad/s and $\Gamma = 1.0 \times 10^8$ rad/s so that $n_r = -1.00$ and $n_i = 1.06 \times 10^{-3}$ at the target frequency $f_0 = 30$ GHz. The electric fields at the center of the slab and 10 cells beyond it, i.e., $E_x(z = 130\Delta z, t)$ and $E_x(z = 140\Delta z, t)$, were sampled. The very early-time responses of these measurements are shown in Fig. 6(a). It is clear that the response of the field at the first point $z_1 = 130\Delta z$ occurs before the one at the second point $z_2 = 140\Delta z$. This demonstrates that causality in the direction of wave propagation is indeed preserved in the DNG medium. The later-time results at the same points are shown in Fig. 6(b). The negative index of refraction nature of the DNG medium is clearly seen. The response at $z_2 = 140\Delta z$ leads the one at $z_1 = 130\Delta z$. The negative index of refraction expresses itself after only a few cycles.

To calculate the index of refraction, Fourier transforms of the two electric field time histories were taken. The time

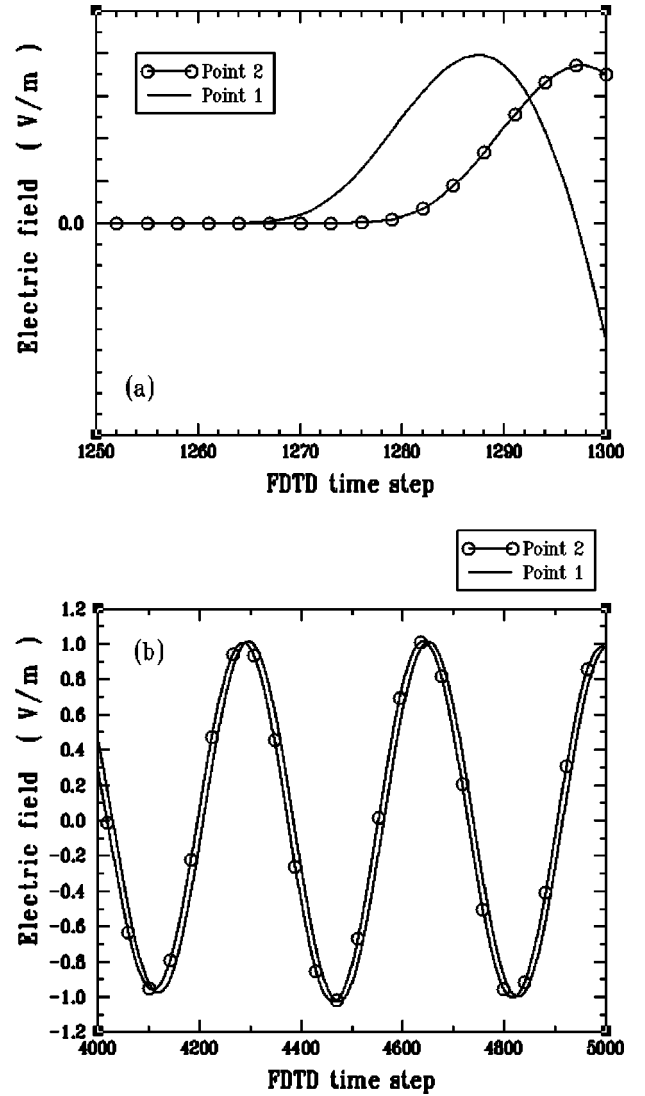


FIG. 6. FDTD predicted electric field time histories at two points: point 1 with $z = 130\Delta z$, 50 cells into the DNG medium, and point 2 with $z = 140\Delta z$. The DNG medium is specified by $\omega_p = 2.665 \times 10^{11}$ rad/s and $\Gamma = 1.0 \times 10^8$ rad/s to give $n_r(f_0) \approx -1.00$. (a) Early-time results; (b) late-time results.

histories contained 20 000 FDTD time steps and were then zero-padded out to 32 768 time points. The discrete Fourier transforms were calculated and are labeled as $\tilde{E}_x(z, \omega)$. We then considered the quantity

$$n_{FDTD} = \frac{1}{ik_0(z_2 - z_1)} \ln \left[\frac{\tilde{E}_x(z_2, \omega)}{\tilde{E}_x(z_1, \omega)} \right]. \quad (33)$$

The values $\text{Re } n_{FDTD} = -1.00$ and $\text{Im } n_{FDTD} = 1.07 \times 10^{-3}$ were obtained for $f = f_0$. The agreement is very good and further confirms the presence of the negative index of refraction for the DNG medium.

Note, however, that in contrast to the description in [4], the wave in the medium travels away from the source in a direction opposite to the direction determined by the negative index. Causality, i.e., the wave propagating away from

the source, does remain intact despite the presence of what appears to be a wave propagating in the DNG medium toward the source.

The 1D FDTD numerical results essentially confirm that the correct choice for the square root is indeed Eq. (9). The wave physics in a DNG medium is thus described by all of the expressions associated with that choice.

IV. FOCUSING PROPERTIES OF A DOUBLE NEGATIVE SLAB

We consider the focusing of point sources through a DNG slab of width d located between $z=0$ and $z=d$. It is sufficient to explore the focusing properties for the TM and TE Green's functions, defined by the equations ([13], Sec. 2.3 or 5.2)

$$[\nabla^2 + k^2(z)]G(\mathbf{r}, \mathbf{r}') = -\delta(\mathbf{r} - \mathbf{r}') \quad (34)$$

subject to the continuity conditions

$$G^{TM} \text{ and } \epsilon^{-1} \partial_z G^{TM} \text{ are continuous at } z_i, \quad (35a)$$

$$G^{TE} \text{ and } \mu^{-1} \partial_z G^{TE} \text{ are continuous at } z_i, \quad (35b)$$

where z_i are the points of any discontinuity in the medium.

These functions may be used to describe the field of any other source configuration. For example, the field due to a longitudinal dipole source

$$\mathbf{J}(\mathbf{r}) = \hat{\mathbf{z}} I_0 \delta(\mathbf{r} - \mathbf{r}') \quad (36)$$

located at $\mathbf{r}' = (0, 0, z_0)$, $z_0 < 0$, is given by [[13], Sec. 5.2, Eqs. (1) and (4c)]

$$\mathbf{E}(\mathbf{r}) = I_0 \frac{1}{-i\omega\epsilon(z)} \nabla \times \nabla \times \hat{\mathbf{z}} G^{TM}, \quad (37a)$$

$$\mathbf{H}(\mathbf{r}) = I_0 \nabla \times \hat{\mathbf{z}} G^{TM}. \quad (37b)$$

Henceforth we shall consider only G^{TM} and remove the superscript TM . It can be synthesized by plane wave superposition

$$G(\mathbf{r}, \mathbf{r}') = \frac{1}{(2\pi)^2} \int dk_x dk_y e^{i(k_x x + k_y y)} g(z, z'; k_t), \quad (38)$$

where $k_t = \sqrt{k_x^2 + k_y^2}$ and

$$\left[\frac{d^2}{dz^2} + k^2 - k_t^2 \right] g(z, z'; k_t) = -\delta(z - z') \quad (39)$$

subject to the same boundary conditions as in Eq. (35b).

The spectral wave numbers and wave impedances in free space and in the slab are

$$\kappa_0 = \sqrt{k_0^2 - k_t^2}, \quad Z_0 = \frac{\kappa_0}{\omega \epsilon_0}, \quad (40a)$$

$$\kappa = \sqrt{k_0^2 n^2 - k_t^2}, \quad Z = \frac{\kappa}{\omega \epsilon}. \quad (40b)$$

The reflection and transmission coefficients of the interface from the double negative medium into air are

$$r = \frac{Z_0 - Z}{Z_0 + Z}, \quad t = 1 + r = \frac{2Z_0}{Z_0 + Z}. \quad (41)$$

The $ABCD$ matrix analysis in [14], Sec. 3.7, and in particular Eq. (3.56) there for R and T , gives the reflection and transmission coefficients from the slab:

$$R(k_t) = \frac{-i \frac{1}{2} \sin \psi (Z/Z_0 - Z_0/Z)}{\cos \psi - i \frac{1}{2} \sin \psi (Z/Z_0 + Z_0/Z)}, \quad (42a)$$

$$T(k_t) = \frac{1}{\cos \psi - i \frac{1}{2} \sin \psi (Z/Z_0 + Z_0/Z)}, \quad (42b)$$

where $\psi = \kappa d$. Note that r and t are subject to the definition of the square roots, because Z is. On the other hand, both R and T are independent of these definitions because they are even functions of κ .

The solution for g is now given by

$$g = \begin{cases} \frac{e^{i\kappa_0|z-z_0|}}{-2i\kappa_0} - R \frac{e^{i\kappa_0(|z_0|-z)}}{-2i\kappa_0}, & z < 0, \\ \frac{e^{i\kappa_0|z_0|}}{-2i\kappa_0} T \frac{Z_0}{iZ} \{e^{i\kappa(z-d)} - r e^{-i\kappa(z-d)}\} = \frac{e^{i\kappa_0|z_0|}}{-2i\kappa_0} T \left\{ \cos \kappa(z-d) + i \frac{Z_0}{Z} \sin \kappa(z-d) \right\}, & 0 < z < d, \\ \frac{1}{-2i\kappa_0} e^{i\kappa_0(z-d+|z_0|)} T, & z > d. \end{cases} \quad (43a)$$

$$g = \begin{cases} \frac{e^{i\kappa_0|z-z_0|}}{-2i\kappa_0} - R \frac{e^{i\kappa_0(|z_0|-z)}}{-2i\kappa_0}, & z < 0, \\ \frac{e^{i\kappa_0|z_0|}}{-2i\kappa_0} T \frac{Z_0}{iZ} \{e^{i\kappa(z-d)} - r e^{-i\kappa(z-d)}\} = \frac{e^{i\kappa_0|z_0|}}{-2i\kappa_0} T \left\{ \cos \kappa(z-d) + i \frac{Z_0}{Z} \sin \kappa(z-d) \right\}, & 0 < z < d, \\ \frac{1}{-2i\kappa_0} e^{i\kappa_0(z-d+|z_0|)} T, & z > d. \end{cases} \quad (43b)$$

$$g = \begin{cases} \frac{e^{i\kappa_0|z-z_0|}}{-2i\kappa_0} - R \frac{e^{i\kappa_0(|z_0|-z)}}{-2i\kappa_0}, & z < 0, \\ \frac{e^{i\kappa_0|z_0|}}{-2i\kappa_0} T \frac{Z_0}{iZ} \{e^{i\kappa(z-d)} - r e^{-i\kappa(z-d)}\} = \frac{e^{i\kappa_0|z_0|}}{-2i\kappa_0} T \left\{ \cos \kappa(z-d) + i \frac{Z_0}{Z} \sin \kappa(z-d) \right\}, & 0 < z < d, \\ \frac{1}{-2i\kappa_0} e^{i\kappa_0(z-d+|z_0|)} T, & z > d. \end{cases} \quad (43c)$$

Because R and T are symmetrical in κ and in Z , as is the field term in the slab region, the solution (41)–(43) is independent of either analytic continuation choice of the sign in the square root for the DNG slab; i.e., κ and Z appear with opposite signs for either choice. This formulation is therefore a convenient starting point to explore the effects of the DNG slab.

A. Solution in a matched DNG slab

Specifically, if one takes a slab matched to free space so that

$$\bar{\epsilon} = \bar{\mu}, \quad (44)$$

then, denoting the standard definition (i.e., with positive real part) of the square root in Eq. (40b) as $\tilde{\kappa}$, we find that $\kappa \rightarrow \mp \tilde{\kappa}$ and $Z \rightarrow \pm Z_0$ where the upper and lower signs cor-

respond to the definition of the square root in Eq. (9) and in Eq. (10), respectively. Thus, *regardless* of the choice of the square root, Eq. (42) becomes

$$R=0, \quad T = [\cos \tilde{\kappa}d + i \sin \tilde{\kappa}d]^{-1} = e^{-i\tilde{\kappa}d}. \quad (45)$$

Note explicitly that for the choice (9) one has $Z = +Z_0$ so that $r=0$ and $t=1$, while for the choice (10) one has $Z = -Z_0$ so that $r=\infty$ and $t=\infty$. Consequently, for either choice of the square root, Eq. (43) yields

$$g = \begin{cases} \frac{e^{i\kappa_0|z-z_0|}}{-2i\kappa_0}, & z < 0, \\ \frac{e^{i\kappa_0|z_0|}}{-2i\kappa_0} e^{-i\tilde{\kappa}d} e^{-i\tilde{\kappa}(z-d)} = \frac{1}{-2i\kappa_0} e^{+i(\kappa_0|z_0| - \tilde{\kappa}z)}, & 0 < z < d, \\ \frac{1}{-2i\kappa_0} e^{i[\kappa_0(z+|z_0|-d) - \tilde{\kappa}d]}, & z > d. \end{cases} \quad (46a)$$

$$\frac{e^{i\kappa_0|z_0|}}{-2i\kappa_0} e^{-i\tilde{\kappa}d} e^{-i\tilde{\kappa}(z-d)} = \frac{1}{-2i\kappa_0} e^{+i(\kappa_0|z_0| - \tilde{\kappa}z)}, \quad 0 < z < d, \quad (46b)$$

$$\frac{1}{-2i\kappa_0} e^{i[\kappa_0(z+|z_0|-d) - \tilde{\kappa}d]}, \quad z > d. \quad (46c)$$

Thus, one does find that the slab solution is completely independent of the choice of the square root. Inside the slab, the phase progression is negative as implied by Eq. (46b).

Now consider, as did Pendry in [3], the lossless, dispersionless case for which $\bar{\epsilon} = \bar{\mu} = -1$ so that $\tilde{\kappa} = \kappa_0$. Equations (46b) and (46c) become

$$g = \begin{cases} \frac{1}{-2i\kappa_0} e^{+i\kappa_0(|z_0|-z)}, & 0 < z < d, \\ \frac{1}{-2i\kappa_0} e^{i[\kappa_0(z+|z_0|-2d)]}, & z > d. \end{cases} \quad (47a)$$

$$\frac{1}{-2i\kappa_0} e^{i[\kappa_0(z+|z_0|-2d)]}, \quad z > d. \quad (47b)$$

Then one observes that the arguments of the exponentials in Eqs. (47a) and (47b) vanish at the points

$$z_{f1} = |z_0|, \quad z_{f2} = 2d - |z_0|. \quad (48)$$

Thus, if $|z_0| < d$, then the field in the slab and the transmitted field beyond the slab have perfect foci at z_{f1} and z_{f2} , respectively. The final field description within this DNG slab consists of a single wave species whose phase propagation direction is backward with focus at point $z = |z_0|$. As a result, the field for $z > d$ focuses again at $z = 2d - |z_0|$. This observation applies for both the propagating spectrum and the evanescent spectrum. The ray picture is thus as seen in Fig. 1

of [3]. The presence of the foci results from the negative index of refraction which causes the transmitted angle to be negative, i.e., in this case

$$\theta_{trans} = \sin^{-1} \left[\frac{\sin \theta_{inc}}{n} \right] = -\theta_{inc}, \quad (49)$$

so that the incident and transmitted rays are located on the same side of the normal to the interface rather than on opposite sides. Yet the arrow directions on these rays are open for interpretation. One may associate the arrows with the energy direction (as in Pendry's paper) but one may alternatively choose to associate them with the phase progression, giving the opposite direction. The analysis above, however, does not assume a specific choice of the square root and thus of the "ray directions." Note also that Pendry's choices for the square roots in [3] for the propagating and evanescent spectra were not consistent. Different choices were made for these two spectra. Our derivation is complete and is independent of the square root definitions.

Next, consider the more general case in Eq. (44) where $\bar{\epsilon} = \bar{\mu} \neq -1$. Here the phases in Eq. (46) do not vanish identically at a given point and the focusing effect is lost. However, we shall explore the possible focusing of the paraxial spectrum components (small k_t/k_0) for which

$$\kappa_0 \approx k_0 - \frac{k_t^2}{2k_0}, \quad \tilde{\kappa} \approx k_0 \tilde{n} - \frac{k_t^2}{2k_0 \tilde{n}}, \quad (50)$$

where, following the definition of $\tilde{\kappa}$ as explained before Eq. (45), \tilde{n} denotes the standard (positive real part) square root of n (i.e., \tilde{n} is positive in the lossless DNG medium and has a negative imaginary part for the lossy case). Expressions (46b) and (46c) become, respectively,

$$g \approx \begin{cases} \frac{1}{-2ik_0} e^{+ik_0(|z_0|-\tilde{n}z)} e^{-i(k_t^2/2k_0)(|z_0|-z/\tilde{n})}, & 0 < z < d, \\ g \approx \frac{1}{-2ik_0} e^{+ik_0[z+|z_0|-d(1+\tilde{n})]} e^{-i(k_t^2/2k_0)[z+|z_0|-d(1+1/\tilde{n})]}, & z > d. \end{cases} \quad (51a)$$

$$g \approx \frac{1}{-2ik_0} e^{+ik_0[z+|z_0|-d(1+\tilde{n})]} e^{-i(k_t^2/2k_0)[z+|z_0|-d(1+1/\tilde{n})]}, \quad z > d. \quad (51b)$$

Thus, the paraxial components may focus at

$$z_{f1} = \tilde{n}|z_0|, \quad z_{f2} = d(1+1/\tilde{n}) - |z_0|, \quad (52)$$

provided, of course, that $z_{f1} < d$ and $z_{f2} > d$. Note that these ‘‘paraxial foci’’ become the ‘‘perfect foci’’ of Eq. (48) when $\tilde{n} \rightarrow 1$. Also note that for a DNG slab with a large negative index of refraction, these paraxial focus locations would be very difficult to distinguish from any interface effects; i.e., as $\tilde{n} \rightarrow \infty$, a paraxial focus at $z_{f1} = d/2$ can be achieved only if $|z_0| = d/(2\tilde{n}) \rightarrow 0$ and hence $z_{f2} \rightarrow d$.

Finally, let us return to the focusing issue from the perspective of the DNG Drude medium. In that case, one has

$$\kappa = \sqrt{\kappa_0^2 - 2 \frac{\omega_p^2}{c^2} \left[\frac{\omega}{\omega + i\Gamma} - \frac{1}{2} \frac{\omega_p^2}{(\omega + i\Gamma)^2} \right]}. \quad (53)$$

Again, the phases in Eq. (46) do not vanish identically at a given point, and the focusing effect is indeed lost. However, in this case the dispersive nature of the medium contributes significantly to the loss of any focusing.

B. Solution in a lossy DNG slab

Recalling next that [4] shows that a lossless, dispersionless DNG medium such as $n(\omega) = -1$ is not physically realizable, we consider the lossy DNG Drude slab. Expressions (52) for the foci are still valid but they become complex and hence there are no real foci and the lens effect is completely lost. However, since the foci are located at complex points, one might expect that the resulting fields will take on beam-like forms, i.e., a point source located at a complex position produces a Gaussian beam field locally [15].

We therefore consider a so-called complex source beam, which is generated by a source at

$$\mathbf{r}' = (0, 0, a \pm ib), \quad b > 0. \quad (54)$$

The field due to this source is a globally exact beam solution of the wave equation that is confined essentially near the z axis. Here, however, we consider only the paraxial regime near this axis where the solution due to the source (54) being located in uniform free space is given by

$$G = \frac{e^{ik|\mathbf{r}-\mathbf{r}'|}}{|\mathbf{r}-\mathbf{r}'|} \approx [\pm(z-a) - ib]^{-1} \exp \left\{ ik \left[(\pm[z-a] - ib) + \frac{1}{2} \frac{x^2 + y^2}{\pm[z-a] - ib} \right] \right\}. \quad (55)$$

This expression is readily recognized as a Gaussian beam field that propagates along the $\pm z$ axis, with a waist

$$W_a = \sqrt{b/k} \quad \text{at } z = a \quad (56)$$

and collimation length $2b$. Furthermore, referring to the spectral representation in Eq. (38), the paraxial expression for the spectrum of the fields in Eq. (55) is given by

$$g \approx \frac{1}{-2ik_0} e^{+i[k_0 - (k_t^2/2k_0)][\pm(z-a) - ib]}. \quad (57)$$

Thus the beam parameters in the lossy DNG medium and, in particular, the waist width may readily be obtained by comparing Eq. (51) with Eq. (57). To this end Eq. (51) is rewritten here as

$$g = \frac{1}{-2ik_0} e^{+ik_0\tilde{n}(-z+|z_0|/\tilde{n})} \times \exp \left\{ -i \frac{k_t^2}{2k_0\tilde{n}} [-(z-|z_0|\tilde{n}_r) - i|z_0|\tilde{n}_i] \right\}, \quad 0 < z < d, \quad (58a)$$

$$g = \frac{1}{-2ik_0} e^{+ik_0[z+|z_0|-d(1+\tilde{n})]} \times \exp \left\{ -i \frac{k_t^2}{2k_0} \left[z+|z_0|-d \left(1 + \frac{\tilde{n}_r}{|\tilde{n}|^2} \right) - id \frac{\tilde{n}_i}{|\tilde{n}|^2} \right] \right\}, \quad z > d, \quad (58b)$$

where we have used explicitly $\tilde{n} = \tilde{n}_r - i\tilde{n}_i$, recalling the definition of \tilde{n} in Eq. (50) with $\tilde{n}_r > 0$ and $\tilde{n}_i > 0$. Comparing the quadratic terms in Eqs. (58a) and (57), one concludes that this expression represents a beam that propagates along the negative z axis in a medium with \tilde{n} and has its waist at $a = |z_0|\tilde{n}_r$ and its collimation length $b = +|z_0|\tilde{n}_i > 0$. Expression (58b) represents a beam that propagates in free space

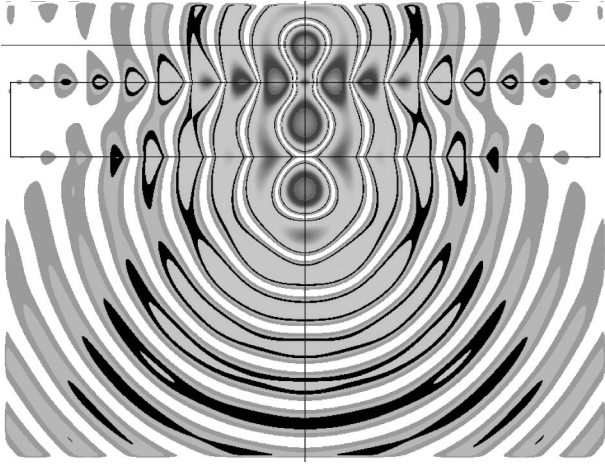


FIG. 7. The electric field intensity over the FDTD simulation space at $t=3900\Delta t$ for the lossless $\omega_p=2.655\times 10^{11}$ rad/s and $\Gamma=0.0$ DNG slab. The DNG slab is outlined and the source is located at the intersection of the horizontal and vertical lines.

along the positive z axis and has its waist at $a=d(1+\tilde{n}_r/|\tilde{n}|^2)-|z_0|$ and its collimation length $b=+d\tilde{n}_i/|\tilde{n}|^2>0$.

C. 2D FDTD simulations

The 2D FDTD simulator solved the equivalent TM set for E_y , H_x , and H_z . These equations were again discretized with a standard leapfrog in time, staggered grid approach. Square FDTD cells were used. The magnetic fields were taken at the cell edges; the electric field was taken at the cell centers. The magnetic and electric currents were taken at the cell centers. Thus, in contrast to the 1D case, the appropriate averaging occurred here in the magnetic field and current equations.

The x - z FDTD simulation space was 820 cells in the \hat{x} and 620 cells in the \hat{z} direction for the lossless DNG Drude case and 820 cells \times 320 cells for the lossy DNG Drude cases reported below. The cell sides were $\Delta x=\Delta z=0.01$ cm long, corresponding to $\lambda_0/100$. The time step was set to be $\Delta t=0.95\Delta z/(\sqrt{2}c)=223.917\times 10^{-15}$ s = 0.224ps. The FDTD grid was terminated with a 10-cell-layer, two-time-derivative Lorentz material (2TDLM) ABC

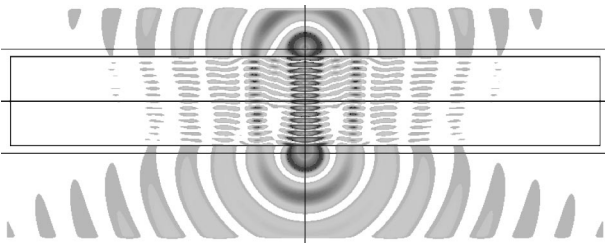


FIG. 8. The electric field intensity over the FDTD simulation space at $t=3900\Delta t$ for the $\omega_p=5.0\times 10^{11}$ rad/s and $\Gamma=1.0\times 10^8$ rad/s DNG slab. The DNG slab is outlined and the source and the paraxial foci locations are located at the intersection of the horizontal and vertical lines.

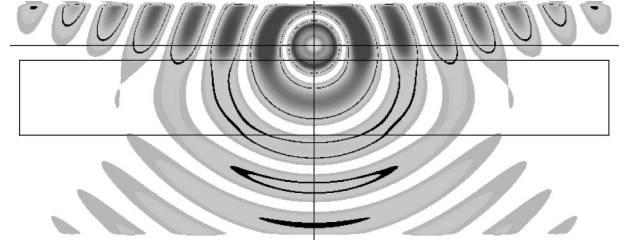


FIG. 9. The electric field intensity over the FDTD simulation space at $t=3700\Delta t$ for the $\omega_p=1.0\times 10^{11}$ rad/s and $\Gamma=1.0\times 10^8$ rad/s DNG slab. The DNG slab is outlined and the source is located at the intersection of the vertical and horizontal lines.

[16–18]. The index labels were K and J , respectively, for the \hat{x} and \hat{z} directions. The line source was located at $K=410$, $J=60$ in all cases. The DNG medium parameters were again those shown in Fig. 1, except for the lossless case in which the $\omega_p=2.665\times 10^{11}$ rad/s case was used with $\Gamma=0.0$. In the intensity figures below gray-scale contours represent different levels. The darker (lighter) regions correspond to higher (lower) intensity levels. In the Poynting vector figures below, the darker (lighter) regions correspond to higher (lower) magnitude values. In both types of figure, some of the contours in regions of expected low values are unavoidably black in order to achieve the targeting lines and the slab outline. Note that the line source takes a time derivative of whatever excitation signal is specified. The single cycle, 20-cycle, and cw pulses were used to investigate the wave propagation effects in the DNG slab. The amplitude of the excitation was normalized by $1/350\times 10^{-6}$ to compensate for the change in the incident pulse amplitude caused by the time derivative. The line source was driven with the cw pulse for all of the cases reported below.

In an attempt to view the perfect lens foci, a lossless DNG Drude slab with $\omega_p=2.665\times 10^{11}$ rad/s and $\Gamma=0.0$ was considered. The DNG slab was located in the cell region $K=[12,808]$ and $J=[110,210]$. The slab was thus $d=100\Delta z$ thick in the direction of propagation and the source-to-slab distance was $|z_0|=50\Delta z<d$. Thus, the conditions specified by the analytical solutions for the foci (48) inside and outside the DNG slab geometry were met. Note that the line source was placed at 50 cells from the front of

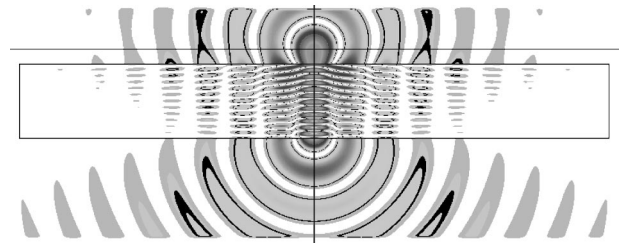


FIG. 10. The electric field intensity over the FDTD simulation space at $t=3700\Delta t$ for the $\omega_p=5.0\times 10^{11}$ rad/s and $\Gamma=1.0\times 10^8$ rad/s DNG slab. The DNG slab is outlined and the source is located at the intersection of the vertical and horizontal lines.

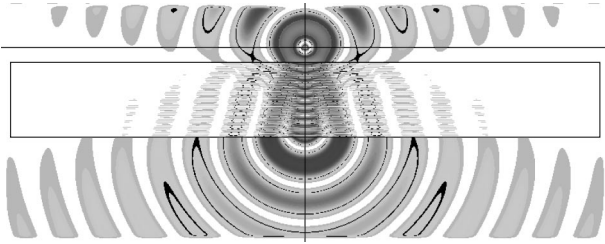


FIG. 11. The electric field intensity over the FDTD simulation space at $t=3900\Delta t$ for the $\omega_p=1.0\times 10^{12}$ rad/s and $\Gamma=1.0\times 10^8$ rad/s DNG slab. The DNG slab is outlined and the source is located at the intersection of the vertical and horizontal lines.

this DNG slab with the hope that the focus in the slab would occur at the center of the slab, 50 cells beyond the front of the slab, and that the focus outside the slab would occur at 50 cells beyond the back of the slab along the z axis. The electric field intensity E_y^2 in the FDTD simulation space at $t=3900\Delta t$ is given in Fig. 7. The FDTD problem space was increased in size in this case with the hope of seeing the wave dynamics better, particularly any misplaced foci. While something like large amplitude fields occur in the neighborhood of the expected foci as shown in Fig. 7, these locations vary dramatically over time, sometimes even completely disappearing. No steady state foci were found. This behavior is symptomatic of the highly dispersive nature of this DNG medium as discussed in Sec. (IV A). Thus, despite numerous attempts with the lossless cases, Pendry's lens effect was not found for this $\bar{\epsilon}_r=\bar{\mu}_r=-1$ case. In fact, almost identical results were obtained for the slightly lossy $\omega_p=2.665\times 10^{11}$ rad/s and $\Gamma=1.0\times 10^8$ rad/s DNG slab. The defocusing is inherent in any realistic DNG medium.

In an attempt to view the paraxial foci, the lossy DNG Drude slab with $\omega_p=5.0\times 10^{11}$ rad/s and $\Gamma=1.0\times 10^8$ rad/s was considered. The DNG slab was located in the cell region $K=[12,808]$ and $J=[70,190]$. The slab was thus $d=120\Delta z$ thick in the direction of propagation and the source-to-slab distance was $|z_0|=10\Delta z < d$. Thus, the conditions specified by the analytical solutions for the paraxial foci (52) are $z_{f1}=\tilde{n}|z_0|\approx 60\Delta z$ and $z_{f2}=d(1+1/\tilde{n})-|z_0|=130\Delta z$ from the front of the DNG slab. The first paraxial focus should therefore appear near the center of the DNG slab, and the second should appear 10 cells beyond its back face. The numerical intensity of the electric field E_y^2 in the FDTD simulation space at $t=3900\Delta t$ is plotted in Fig. 8. The locations of the source and the paraxial foci are noted. One does observe a paraxial focus near the center of the DNG slab. As noted in Sec. (IV A), the paraxial focus beyond the rear face is very difficult to distinguish from the behavior of the field as the wave exits the slab. Nonetheless, there is an enhanced field level where it is expected just beyond the rear face.

Finally, it was desired to determine the structure of the fields for cases when no paraxial foci should appear in the DNG slab. The slabs that were simulated were all located in the cell region $K=[12,808]$ and $J=[80,180]$. The slabs were thus $d=100\Delta z$ thick in the direction of propagation

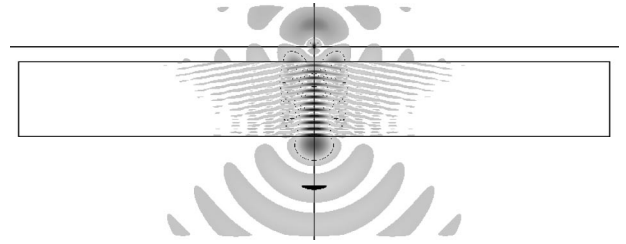


FIG. 12. The term $-E_y H_x$ is plotted over the FDTD simulation space at $t=3750\Delta t$ for the $\omega_p=5.0\times 10^{11}$ rad/s and $\Gamma=1.0\times 10^8$ rad/s DNG slab. The DNG slab is outlined and the source is located at the intersection of the vertical and horizontal lines.

and the source-to-slab distance was $|z_0|=20\Delta z < d$. Slabs with $\omega_p=1.0\times 10^{11}$ rad/s, 5.0×10^{11} rad/s, and 1.0×10^{12} rad/s and $\Gamma=1.0\times 10^8$ rad/s were considered. For all of these cases, the conditions for foci or paraxial foci specified by the analytical solutions for the DNG slab geometry were not met. The numerical intensity of the electric field E_y^2 in the FDTD simulation space is plotted in Figs. 9–11 for these three DNG slabs at the times $t=3700\Delta t$, $t=3700\Delta t$, and $t=3950\Delta t$, respectively. For all of these cases, these observation times represent enough time for many cycles to propagate through the slab and enter back into free space beyond the slab. Recall that Fig. 9 represents the case where the slab has positive permittivity and permeability at the target frequency f_0 . In contrast, Figs. 10 and 11 represent the results for DNG slabs at the target frequency f_0 . As predicted, one finds that there are no focal points in any of these cases. This is particularly obvious in both the regions $0\leq z\leq d$ and $z>d$. These results confirm that a large negative index of refraction, dispersive DNG slab completely lacks the presence of any foci. It was found that the fields were LH with respect to \mathbf{k} , but were RH with respect to the propagation axis $+\hat{z}$, and they were not growing in the $+\hat{z}$ direction as steady state conditions were obtained. While there are no focal points, Figs. 10 and 11 do show a distinctive beamlike channeling of the waves near the normal as the permittivity and permeability become more negative. As the waves reenter free space from the DNG slab, they begin to diverge as though they originate from an extended line source at the rear face of the slab. This channeling of the wave energy within the DNG slab is further described by viewing the

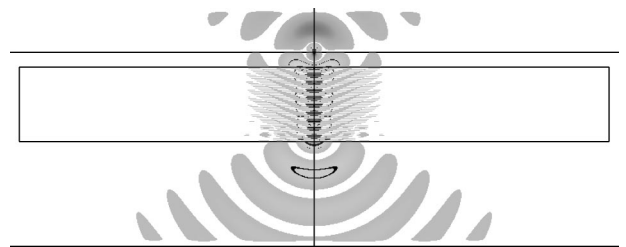


FIG. 13. The term $-E_y H_x$ is plotted over the FDTD simulation space at $t=3750\Delta t$ for the $\omega_p=1.0\times 10^{12}$ rad/s and $\Gamma=1.0\times 10^8$ rad/s DNG slab. The DNG slab is outlined and the source is located at the intersection of the vertical and horizontal lines.

Poynting vector component $-E_y H_x$ which is plotted throughout the simulation space at $t=3750\Delta t$ for the $\omega_p = 5.0 \times 10^{11}$ rad/s case in Fig. 12 and for the $\omega_p = 1.0 \times 10^{12}$ rad/s case in Fig. 13. One can see that the power flow is positive in the DNG slab and is being concentrated along the $+\hat{z}$ axis. Note that in Figs. 12 and 13 the waves along the z axis are traveling at speeds $v_g \ll c$. The waves away from the axis travel faster than those on this axis, which further explains the channeling of the wave energy along the propagation axis. This behavior is readily seen in the time slice shown in Fig. 12.

V. CONCLUSIONS

We have investigated the propagation of electromagnetic waves in DNG media from both analytical and numerical points of view. Analytical continuation based choices of the square roots associated with the index of refraction and the wave impedance were introduced. The wave physics associated with each of these choices was clarified. Results for the 1D plane wave scattering from a DNG interface and a DNG slab and the 2D line source cylindrical wave excitation of the DNG slab were presented. The DNG slab solution was shown to be independent of the choice of the square roots.

Numerical FDTD simulations of these 1D and 2D cases were provided.

It was demonstrated that the choice of the square root that produces a negative index of refraction and positive wave impedance is the correct choice. The presence of the negative index of refraction was shown to be not in disagreement with causality, and its presence was verified with the FDTD simulations. The analytical solution for a matched DNG slab demonstrated that the Pendry “perfect lens” effect can be realized only in the presence of a nondispersive, lossless DNG medium having $\bar{\epsilon} = \bar{\mu} = -1$; i.e., $n(\omega) = -1$. The lens effect was shown not to exist for any realistic dispersive, lossy DNG medium. The FDTD simulations further confirmed this conclusion. No focal points either within the slab or in its exterior were found in any of the FDTD simulations. These simulations did, however, show a channeling or paraxial focusing of the wave energy due to the presence of a DNG slab, particularly when the index of refraction had large negative values. This possibility was correctly predicted by the analytical solution. The DNG slab converted the cylindrical wave into a beamlike field as it propagated through the DNG slab. This channeling effect may have many practical considerations and is being investigated further.

-
- [1] V.G. Veselago, *Sov. Phys. Usp.* **10**, 509 (1966).
 - [2] H. Kosaka, T. Kawashima, A. Tomita, M. Notomi, T. Tamamura, T. Sato, and S. Kawakami, *Phys. Rev. B* **58**, R10 096 (1998).
 - [3] J.B. Pendry, *Phys. Rev. Lett.* **85**, 3966 (2000).
 - [4] D.R. Smith and N. Kroll, *Phys. Rev. Lett.* **85**, 2933 (2000).
 - [5] R.A. Shelby, D.R. Smith, S.C. Nemat-Nasser, and S. Schultz, *Appl. Phys. Lett.* **78**, 489 (2001).
 - [6] R.A. Shelby, D.R. Smith, and S. Schultz, *Science* **292**, 77 (2001).
 - [7] R.W. Ziolkowski, *Phys. Rev. E* **63**, 046604 (2001).
 - [8] J.D. Joannopoulos, R.D. Meade, and J.N. Winn, *Photonic Crystals: Molding the Flow of Light* (Princeton University Press, Princeton, NJ, 1995).
 - [9] J.A. Kong, *Electromagnetic Wave Theory* (John Wiley & Sons, New York, 1986).
 - [10] A. Taflove, *Computational Electrodynamics, The Finite-Difference Time-Domain Method* (Artech House, Inc., Norwood, MA, 1995).
 - [11] *Advances in Computational Electrodynamics: The Finite-Difference Time-Domain Method*, edited by A. Taflove (Artech House, Inc., Norwood, MA, 1998).
 - [12] J.L. Young and R.O. Nelson, *IEEE Antennas Propag. Mag.* **43**, 61 (2001).
 - [13] L.B. Felsen and N. Marcuvitz, *Radiation and Scattering of Waves* (IEEE Press, Piscataway, NJ, 1994).
 - [14] A. Ishimaru, *Electromagnetic Wave Propagation, Radiation and Scattering* (Prentice Hall, Englewood Cliffs, NJ, 1991).
 - [15] G.A. Deschamps, *Electron. Lett.* **7**, 23 (1971).
 - [16] D.C. Wittwer and R.W. Ziolkowski, *IEEE Trans. Antennas Propag.* **48**, 192 (2000).
 - [17] D.C. Wittwer and R.W. Ziolkowski, *IEEE Trans. Antennas Propag.* **48**, 200 (2000).
 - [18] D.C. Wittwer and R.W. Ziolkowski, *IEEE Trans. Microwave Theory Tech.* **49**, 250 (2001).